日本磁気学会
ISSN 2432-0250
Journal of the Magnetics Society of Japan
Electronic Journal URL: https://www.jstage.jst.go.jp/browse/msjmag

Vol.45 No.6　2021

Journal

Thin Films, Fine Particles, Multilayers, Superlattices

JOURNAL OF THE MAGNETICS SOCIETY OF JAPAN

Vol.45 No.6 2021

日本磁気学会

ISSN 2432-0250

HP: http://www.magnetics.jp/ e-mail: msj@bj.wakwak.com
Electronic Journal: http://www.jstage.jst.go.jp/browse/msjmag

Journal of the Magnetics Society of Japan
Vol. 45, No. 6

Electronic Journal URL: https://www.jstage.jst.go.jp/browse/msjmag

CONTENTS

Thin Films, Fine Particles, Multilayers, Superlattices

INDEX

J. Magn. Soc. Jpn., **45**, 136-141 (2021)

<Paper>

Influence of B Content on the Magnetostrictive Properties of Single-Crystalline, Poly-Crystalline, and Amorphous Fe-Co-B Alloy Films

Yuta Nakamura[1], Mitsuru Ohtake[1], Tetsuroh Kawai[1], Masaaki Futamoto[1],
Fumiyoshi Kirino[2], and Nobuyuki Inaba[3]

[1]Faculty of Engineering, Yokohama National University, *79-5 Tokiwadai, Hodogaya, Yokohama 240-8501, Japan*
[2]Graduate School of Fine Arts, Tokyo University of the Arts, *12-8 Ueno-koen, Taito, Tokyo 110-8714, Japan*
[3]Graduate School of Science and Engineering, Yamagata University, *4-3-16 Jyonan, Yonezawa, Yamagata 992-8510, Japan*

$(Fe_{0.7}Co_{0.3})_{100-x}B_x$ (x = 0–15, at. %) alloy films of 100 nm thickness are prepared on VN(001) single-crystalline underlayers at 600 °C and on VN poly-crystalline underlayers at room temperature (RT). A high substrate temperature of 600 °C is used to promote epitaxial film growth on VN(001) underlayer. Influences of B content on the structural, magnetic, and magnetostrictive properties are investigated. The films formed on VN(001) underlayers involve bcc(001) epitaxial crystalline phase, whereas those formed on VN poly-crystalline underlayers consist of poly-crystalline and/or amorphous phases. Surface roughness of film formed on VN(001) underlayer at 600 °C increases with increasing the B content, whereas flat surfaces are realized for the films formed on VN poly-crystalline underlayers at RT. The surface morphology is influenced by both the substrate temperature and the B content. The films with flat surfaces show good soft magnetic properties. In contrast, rough surface causes an increase in the saturation magnetic field. In the case of films formed on VN(001) single-crystalline underlayer at 600 °C, magnetostriction value of λ_{100} increases from $+200 \times 10^{-6}$ to $+310 \times 10^{-6}$, as the B content increases from x = 0 to 5. With further increasing the B content, λ_{100} value decreases due to unsaturation of magnetization at a magnetic field of 1200 Oe which is the maximum value used for measurement. λ_{111} values are nearly zero (-10×10^{-6} – $+20 \times 10^{-6}$) for all the investigated B contents. Slight addition of B atoms around 5 at. % is effective in enhancing the λ_{100} value, while keeping high crystallographic quality, flat surface, and soft magnetic property. On the contrary, the films formed on VN poly-crystalline underlayers at RT show moderately large λ values of about $+60 \times 10^{-6}$ for all the B contents. The present study shows that control of B content and realization of flat surface are important factors in enhancing the magnetostriction of Fe-Co-B film.

Keywords: Fe-Co-B alloy, single-crystal, poly-crystal, amorphous, thin film, magnetostriction

1. Introduction

Fe-Co alloys have recently attracted much attention as one of magnetostrictive materials, since they show large saturation magnetization (M_s) values[1)] of about 1920 emu/cm^3, low magnetocrystalline anisotropy energies[2)] around 0 erg/cm^3, and large magnetostriction (λ) values[3)–7)] of $+100 \times 10^{-6}$ – $+250 \times 10^{-6}$ by optimizing the composition. Furthermore, it has been reported that large λ values of $+150 \times 10^{-6}$ – $+250 \times 10^{-6}$ can be obtained in poly-crystalline Fe-Co films with Co contents of 35–75 at. % prepared by deposition at room temperature (RT) followed by annealing at 800 °C[8)].

In order to determine the magnetostriction values along <100> and <111>, λ_{100} and λ_{111}, it is required to prepare single-crystalline samples. Epitaxial films are candidates for such purpose. In our previous study[9)], Fe-Co single-crystalline films were prepared on MgO(001) substrates at 300 °C by varying the Co content from 0 to 50 at. %. λ_{100} value increased with increasing the Co content. λ_{100} values larger than $+230 \times 10^{-6}$ were observed for the films with Co content higher than 30 at. %. The λ_{111} value of $Fe_{70}Co_{30}$ film was nearly zero.

In order to obtain a good soft magnetic property, it seems useful to control the Co content to be around 30–40 at. %, because the magnetocrystalline anisotropy energy is almost zero. Furthermore, B is often added to Fe-Co alloy to improve the soft magnetic property. The magnetostrictive properties of Fe-Co-B alloys have been studied by using film[10)–13)] and ribbon[14)–15)] samples consisting of poly-crystalline or amorphous phase. There is a possibility that B atom addition may enhance the magnetostriction, similar to the case of Fe-B alloy. However, there are no reports on systematical investigation on magnetostrictive properties by using single-crystalline, poly-crystalline, and amorphous specimens.

The purpose of present study is to prepare single-crystalline, poly-crystalline, and amorphous $(Fe_{0.7}Co_{0.3})_{100-x}B_x$ films with different B contents and to investigate the magnetostrictive properties. In the present study, $(Fe_{0.7}Co_{0.3})_{100-x}B_x$ films are formed on VN(001) single-crystalline underlayers at 600 °C for preparation of single-crystalline $(Fe_{0.7}Co_{0.3})_{100-x}B_x$ films. A high substrate temperature of 600 °C is used to promote epitaxial growth on VN(001) underlayer. $(Fe_{0.7}Co_{0.3})_{100-x}B_x$ films are also formed on VN poly-crystalline underlayers at RT for preparation of poly-crystalline and/or amorphous $(Fe_{0.7}Co_{0.3})_{100-x}B_x$ films. When growth of a film on an underlayer follows the Volmer-Weber mode[16)], the film consists of islands. The contact angle of island with respect to the underlayer is influenced by the combination of surface energies of film and underlayer (Young's relation). In

---

Corresponding author:
Mitsuru Ohtake (e-mail: ohtake-mitsuru-yt@ynu.ac.jp).

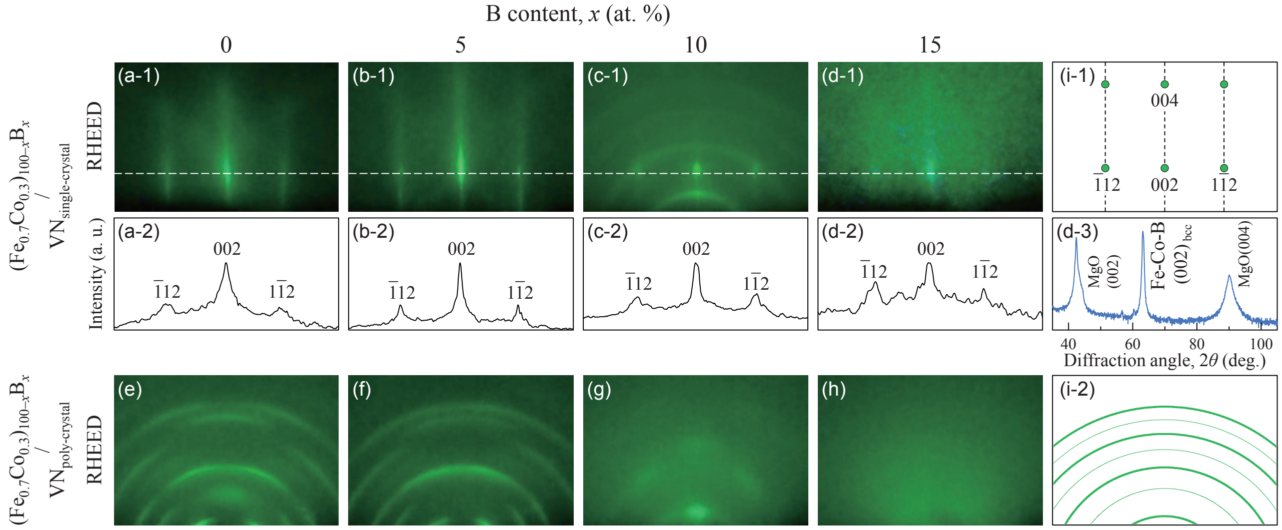

Fig. 1 [(a-1)–(d-1), (e)–(h)] RHEED patterns observed for $(Fe_{0.7}Co_{0.3})_{100-x}B_x$ films of 100 nm thickness with x = [(a-1), (e)] 0, [(b-1), (f)] 5, [(c-1), (g)] 10, and [(d-1), (h)] 15 formed (a-1)–(d-1) on VN(001) single-crystalline underlayers at 600 °C and (e)–(h) on VN poly-crystalline underlayers at RT. (a-2)–(d-2) Line profiles measured along the dotted lines in RHEED patterns of (a-1)–(d-1), respectively. (d-3) XRD pattern measured for the $(Fe_{0.7}Co_{0.3})_{100-x}B_x$ film with x = 15 formed on VN(001) single-crystalline underlayer. (i) Schematic diagrams of RHEED patterns simulated for (i-1) (001) single-crystalline and (i-2) poly-crystalline surfaces with bcc structure. The incident electron beam is parallel to (a-1)–(d-1) VN[100] (∥ MgO[100]) or (i-1) bcc[110].

order to suppress the surface undulation, it is useful to employ an underlayer material whose surface energy is larger than that of film material. The surface energy of VN crystal (2.7 J/m^2)17) is higher than that of Fe crystal (2.2 J/m^2)18), though there are, to our knowledge, no reports on the surface energy of $Fe_{70}Co_{30}$ crystal. Introduction of VN underlayer seems effective to realize flat film surface, similar to the case of $Fe_{50}Pt_{50}$ film on VN underlayer19). VN underlayers are thus introduced in the present study.

2. Experimental Procedure

A radio-frequency (RF) magnetron sputtering system with the base pressure lower than 4 × 10^{-7} Pa was used for film formation. The distance between target and substrate and the Ar gas pressure during sputtering were respectively fixed at 150 mm and 0.67 Pa. $(Fe_{0.7}Co_{0.3})_{100-x}B_x$ (x = 0, 5, 10, and 15 at. %) and VN alloy targets of 3 inch diameter were employed and the respective RF powers were adjusted to 51, 90, 56, 60, and 96 W to make the deposition rate 0.02 nm/s for all the materials. The film compositions were confirmed by energy dispersive X-ray spectroscopy (EDS) and X-ray photoelectron spectroscopy (XPS) and the errors were less than 1.5% from the target compositions.

VN(001) single-crystalline underlayers of 10 nm thickness with $B1$ structure were prepared through hetero-epitaxial growth on MgO(001) substrates of 300 μm thickness in the orientation relationship of VN(001)[100] ∥ MgO(001)[100]19), whereas VN poly-crystalline underlayers of 10 nm thickness were formed on thermally oxidized Si substrates of 350 μm thickness. The substrate temperature during underlayer formation was kept constant at 600 °C for both cases. The arithmetical mean surface roughness (R_a) values of VN single- and poly-crystalline underlayers measured by atomic force microscopy (AFM) were lower than 0.1 nm. Then, $(Fe_{0.7}Co_{0.3})_{100-x}B_x$ films of 100 nm thickness were formed on the VN(001) underlayers at 600 °C and on the VN poly-crystal underlayers at RT.

The structure was studied by reflection high-energy electron diffraction (RHEED) and X-ray diffraction (XRD) with Cu-Kα radiation (wavelength: 0.15418 nm). The surface morphology was observed by AFM. The magnetization curves were measured by vibrating sample magnetometry (VSM). The magnetostriction was evaluated by using a cantilever method under rotating magnetic fields up to 1200 Oe. The relative length variation, $\Delta\ell/\ell$, was calculated from the following formula,

$$\frac{\Delta\ell}{\ell} = \frac{\Delta S\, t_s^2\, E_s\,(1+\nu_f)}{3\,L^2\, t_f\, E_f\,(1-\nu_s)}, \qquad (1)$$

where ΔS is the measured bending, L is the distance between laser beam points (12.5 mm), t is the thickness, E is the Young's modules, ν is Poisson's ratio, and the subscript of s or f respectively refers to substrate or film. The details of our measurement system and calculation are reported in our previous papers9),20).

3. Results and Discussion

3.1 Structure

The structures of $(Fe_{0.7}Co_{0.3})_{100-x}B_x$ films with different B contents prepared on VN single- and poly-crystalline underlayers were studied by RHEED. Figures 1(a-1)–(d-1) show the RHEED patterns observed for $(Fe_{0.7}Co_{0.3})_{100-x}B_x$ films of 100 nm thickness formed on VN(001) single-crystalline underlayers at 600 °C. A diffraction pattern from bcc(001) single-crystalline surface is recognized for the film with x = 0 (Fig. 1(a-1)), as shown in the schematic diagram of

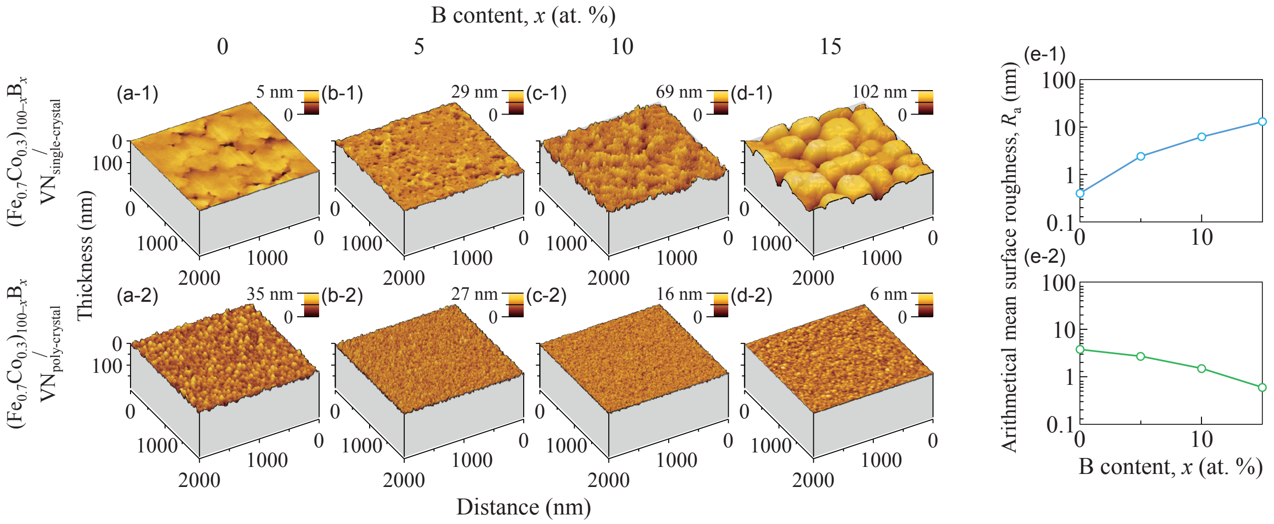

Fig. 2 (a)–(d) AFM images observed for $(Fe_{0.7}Co_{0.3})_{100-x}B_x$ films of 100 nm thickness with x = (a) 0, (b) 5, (c) 10, and (d) 15 formed (a-1)–(d-1) on VN(001) single-crystalline underlayers at 600 °C and (a-2)–(d-2) on VN poly-crystalline underlayers at RT. (e) B content dependences of R_a values of $(Fe_{0.7}Co_{0.3})_{100-x}B_x$ films formed (e-1) on VN(001) single-crystalline underlayer at 600 °C and (e-2) on VN poly-crystalline underlayer at RT.

Fig. 1(i-1). A single-crystalline $Fe_{70}Co_{30}$(001) film is epitaxially grown on the VN underlayer. The crystallographic orientation relationship is determined as $(Fe_{0.7}Co_{0.3})_{100-x}B_x$(001)[110] ‖ VN(001)[100]. A diffraction pattern from bcc(001) surface is also observed for the film with x = 5 (Fig. 1(b-1)). However when the B content increases up to x = 10 (Fig. 1(c-1)), ring-like and halo patterns are overlapped. The result suggests that the film with x = 10 involves poly-crystalline and amorphous phases in addition to bcc(001) crystalline phase. With further increasing the B content to x = 15 (Fig. 1(d-1)), the RHEED pattern is more blurred, though the reflection spots from bcc(001) surface are still appearing as shown in the line profile of RHEED pattern of Fig. 1(d-2). The existence of bcc(001) crystalline phase is also confirmed by XRD, as shown in Fig. 1(d-3). These results indicate that the volume ratio of amorphous to crystalline phase has increased. Although the crystallographic quality deteriorates with increasing the B content, $(Fe_{0.7}Co_{0.3})_{100-x}B_x$ films including bcc(001) crystalline phase are obtained for all the investigated B contents.

Figures 1(e)–(h) show the RHEED patterns observed for $(Fe_{0.7}Co_{0.3})_{100-x}B_x$ films of 100 nm thickness formed on VN poly-crystalline underlayers at RT. A diffraction pattern from bcc poly-crystalline surface is recognized for the films with x = 0 and 5 (Figs. 1(e), (f)), as shown in the schematic diagram of Fig. 1(i-2). The films are composed of bcc poly-crystalline phase. When the B content increases to x = 10 (Fig. 1(g)), a halo pattern is overlapped with a ring-like pattern. The film with x = 10 consists of a mixture of poly-crystalline and amorphous phases. Only a halo pattern is appearing for the film with x = 15 (Fig. 1(h)). Amorphous film is formed at the B content of x = 15. B content dependence of crystallization is similar between the $(Fe_{0.7}Co_{0.3})_{100-x}B_x$ films formed on single- and poly-crystalline underlayers. In detail, however, amorphous phase formation is more pronounced for the films formed on VN poly-crystalline underlayers, which are prepared at a lower substrate temperature of RT.

3.2 Surface morphology and magnetic property

Surface morphologies, which influence the magnetization properties, were observed by AFM. Figures 2(a-1)–(d-1) show the AFM images observed for $(Fe_{0.7}Co_{0.3})_{100-x}B_x$ films formed on VN single-crystalline underlayers at 600 °C. Figure 2(e-1) summarizes the B content dependence of R_a. For the film with x = 0 (Fig. 2(a-1)), a flat surface with the R_a value of 0.4 nm is realized, even though a high substrate temperature of 600 °C is used. However with increasing the B content, wettability of $(Fe_{0.7}Co_{0.3})_{100-x}B_x$ film with respect to VN underlayer gradually deteriorates (Figs. 2(b-1)–(d-1)). R_a value increases to 13 nm with increasing the B content to x = 15. For the film with x = 0, employment of VN underlayer with high surface energy (2.7 J/m^2)[17] is apparently effective in reducing the surface roughness, similar to the case of $Fe_{50}Pt_{50}$ film[19]. The reason for R_a increase with B addition is attributed to an increase of surface energy of $(Fe_{0.7}Co_{0.3})_{100-x}B_x$ alloy material, which is expected from the cases of Ti-B[21),22] and V-B[21),23] alloys. The contact angle between the film and the VN underlayer materials is considered to have increased and the surface roughness is thus enhanced.

Figures 2(a-2)–(d-2) and (e-2), respectively, show the AFM images and the R_a values of $(Fe_{0.7}Co_{0.3})_{100-x}B_x$ films formed on VN poly-crystal underlayers at RT. These films have flatter surfaces, when compared with those of $(Fe_{0.7}Co_{0.3})_{100-x}B_x$ films formed on VN(001) underlayers. The difference is possibly due to the effect of lower deposition temperature of RT. Furthermore, it is noted that lower R_a value is realized with increasing the B content, which is interpreted to be corresponding to the structural variation from crystalline to amorphous phase.

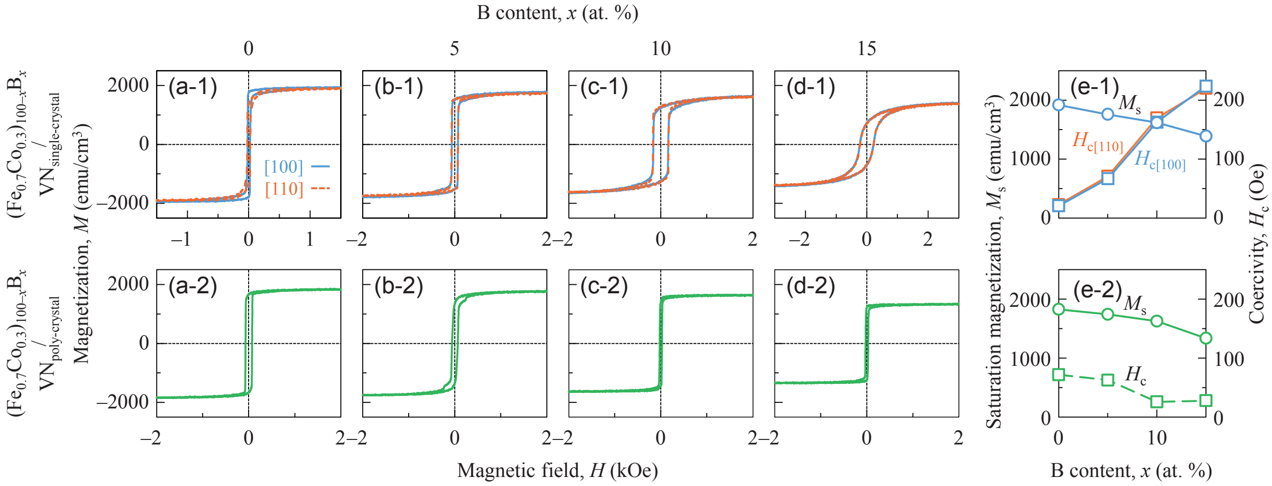

Fig. 3 (a)–(d) In-plane magnetization curves measured for $(\mathrm{Fe}_{0.7}\mathrm{Co}_{0.3})_{100-x}\mathrm{B}_x$ films of 100 nm thickness with x = (a) 0, (b) 5, (c) 10, and (d) 15 formed (a-1)–(d-1) on VN(001) single-crystalline underlayers at 600 °C and (a-2)–(d-2) on VN poly-crystalline underlayers at RT. The magnetic field is applied parallel to $(\mathrm{Fe}_{0.7}\mathrm{Co}_{0.3})_{100-x}\mathrm{B}_x[100]$ (∥ VN[1$\bar{1}$0] ∥ MgO[1$\bar{1}$0]) or $(\mathrm{Fe}_{0.7}\mathrm{Co}_{0.3})_{100-x}\mathrm{B}_x[110]$ (∥ VN[100] ∥ MgO[100]). (e) B content dependences of M_s and H_c values of $(\mathrm{Fe}_{0.7}\mathrm{Co}_{0.3})_{100-x}\mathrm{B}_x$ films formed (e-1) on VN(001) single-crystalline underlayer at 600 °C and (e-2) on VN poly-crystalline underlayer at RT.

Figures 3(a-1)–(d-1) show the in-plane magnetization curves of $(\mathrm{Fe}_{0.7}\mathrm{Co}_{0.3})_{100-x}\mathrm{B}_x$ films involving bcc(001) crystalline phase prepared on VN single-crystalline underlayers. The magnetic field is applied parallel to [100] or [110] direction. The film with x = 0 is easily magnetized when the magnetic field is applied parallel to [100], whereas the magnetization curve measured along [110] saturates at a higher magnetic field (Fig. 3(a-1)). The magnetization behavior is reflecting the magnetocrystalline anisotropy of bulk bcc-$\mathrm{Fe}_{70}\mathrm{Co}_{30}$ crystal with the easy magnetization axes parallel to <100>[5]. On the contrary, the films including B atoms (x = 5–15) show nearly isotropic in-plane magnetic properties (Figs. 3(b-1)–(d-1)). The reason is considered to be partly due to reduction in magnetocrystalline anisotropy energy and structural variation from crystalline to amorphous caused by B addition and partly due to increase in surface roughness which is shown by AFM observation (Figs. 2(b-1)–(d-1)). Figure 3(e-1) shows the B content dependences of M_s and coercivity (H_c) measured for $(\mathrm{Fe}_{0.7}\mathrm{Co}_{0.3})_{100-x}\mathrm{B}_x$ film formed on VN(001) single-crystalline underlayer. With increasing B content, M_s is decreasing, while H_c is increasing. The increase in H_c is attributable to the enhancement of surface roughness that prevents the magnetic domain wall motion.

Figures 3(a-2)–(e-2) show the in-plane magnetization curves and the M_s and H_c values of $(\mathrm{Fe}_{0.7}\mathrm{Co}_{0.3})_{100-x}\mathrm{B}_x$ films consisting of poly-crystalline and/or amorphous phases prepared on VN poly-crystalline underlayers. As the B content increases, M_s value decreases, similar to the case of $(\mathrm{Fe}_{0.7}\mathrm{Co}_{0.3})_{100-x}\mathrm{B}_x$ films formed on VN(001) underlayers. On the contrary, H_c value decreases with increasing the B content, which is different from the case of films formed on VN(001) underlayers. The reduction in H_c seems to be related with the decrease in R_a and the structural variation from crystalline to amorphous phase.

3.3 Magnetostrictive properties

Magnetostrictive behaviors were investigated by using a cantilever method under in-plane rotating magnetic fields. The relative length variations of bcc(001) single-crystal along [100] and [110], $\Delta\ell/\ell_{[100]}(\varphi)$ and $\Delta\ell/\ell_{[110]}(\varphi)$, under an in-plane rotating magnetic field are respectively shown[9] as

$$\frac{\Delta\ell}{\ell}_{[100]}(\varphi) = \frac{3}{4}\lambda_{100}\cos 2\varphi + \frac{1}{4}\lambda_{100}\,, \qquad (2)$$

$$\frac{\Delta\ell}{\ell}_{[110]}(\varphi) = \frac{3}{4}\lambda_{111}\sin 2\varphi + \frac{1}{4}\lambda_{100}\,, \qquad (3)$$

where φ is the angle of magnetic field direction with respect to [100]. $\Delta\ell/\ell_{[100]}(\varphi)$ and $\Delta\ell/\ell_{[110]}(\varphi)$ are cosine and sine waves, whose phases vary depending on the signs of λ_{100} and λ_{111} and whose amplitudes correspond to the absolute values of 3/4 times λ_{100} and λ_{111}, respectively. Figure 4 shows the $\Delta\ell/\ell_{[100]}(\varphi)$ and $\Delta\ell/\ell_{[110]}(\varphi)$ measured for $(\mathrm{Fe}_{0.7}\mathrm{Co}_{0.3})_{100-x}\mathrm{B}_x$ films including bcc(001) crystalline phase prepared on VN(001) underlayers. The amplitudes of $\Delta\ell/\ell_{[100]}(\varphi)$ are fairly larger than those of $\Delta\ell/\ell_{[110]}(\varphi)$ for the respective B contents. The result suggests that the films possess large λ_{100} and small λ_{111}. The phases of $\Delta\ell/\ell_{[100]}(\varphi)$ correspond to positive λ_{100} for all the B contents. On the other hand, the phase of $\Delta\ell/\ell_{[110]}(\varphi)$ is different between the films without and with B atoms. The signs of λ_{111} of films with x = 0 and 5–15 are respectively negative and positive.

The relative length variation of poly-crystalline and/or amorphous phase, $\Delta\ell/\ell_{\text{poly-crystalline/amorphous}}(\psi)$, is shown as

$$\frac{\Delta\ell}{\ell}_{\text{poly-crystalline/amorphous}}(\psi) = \frac{3}{4}\lambda_{\text{poly-crystalline/amorphous}}\cos 2\psi + \frac{1}{4}\lambda_{\text{poly-crystalline/amorphous}}\,, \qquad (4)$$

where $\lambda_{\text{poly-crystalline/amorphous}}$ is the magnetostriction value and ψ is the angle of magnetic field direction with respect to the direction rotated by 45° from the

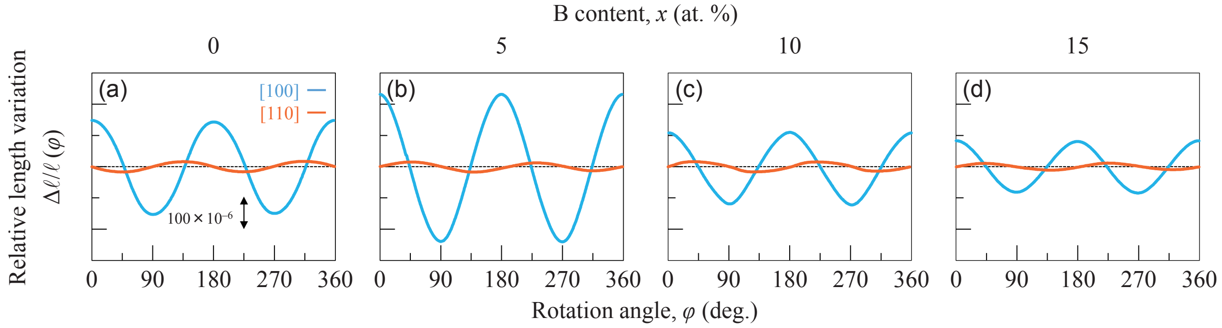

Fig. 4 $\Delta\ell/\ell_{[100]}(\varphi)$ and $\Delta\ell/\ell_{[110]}(\varphi)$ under a rotating magnetic field of 1200 Oe measured for $(\mathrm{Fe}_{0.7}\mathrm{Co}_{0.3})_{100-x}\mathrm{B}_x$ films of 100 nm thickness with x = (a) 0, (b) 5, (c) 10, and (d) 15 involving bcc(001) crystalline phase prepared on VN(001) underlayers. The observation direction is parallel to [100] or [110] of the bcc(001) crystal.

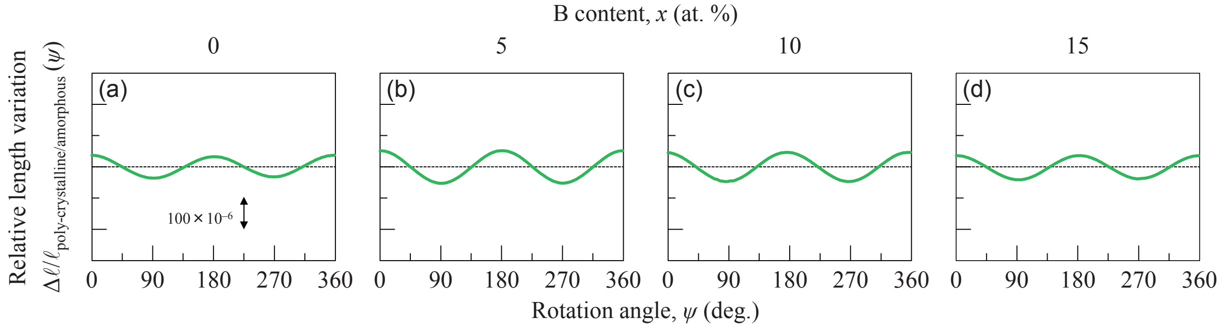

Fig. 5 $\Delta\ell/\ell_{\text{poly-crystalline/amorphous}}(\psi)$ under a rotating magnetic field of 1200 Oe measured for $(\mathrm{Fe}_{0.7}\mathrm{Co}_{0.3})_{100-x}\mathrm{B}_x$ films of 100 nm thickness with x = (a) 0, (b) 5, (c) 10, and (d) 15 consisting of poly-crystalline and/or amorphous phases prepared on VN poly-crystalline underlayers.

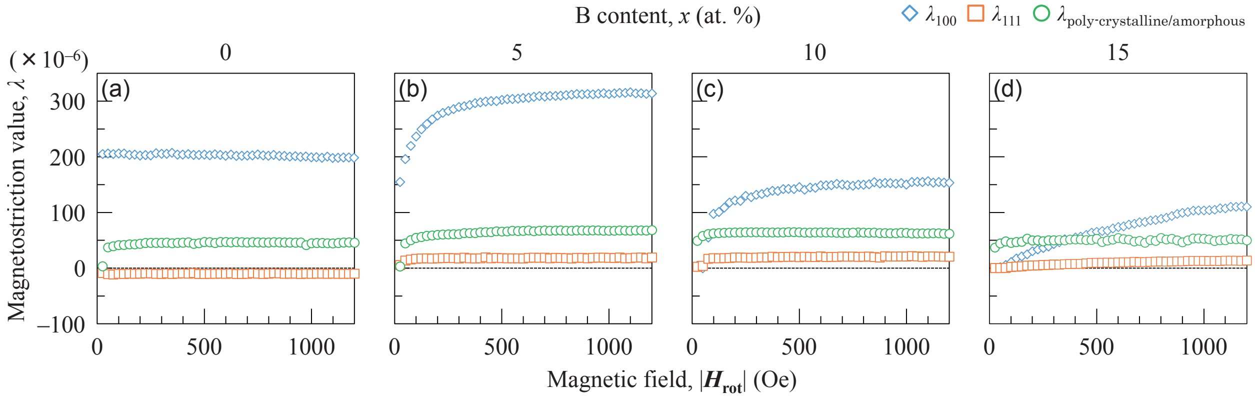

Fig. 6 Magnetic field dependences of λ_{100}, λ_{111}, and $\lambda_{\text{poly-crystalline/amorphous}}$ measured for $(\mathrm{Fe}_{0.7}\mathrm{Co}_{0.3})_{100-x}\mathrm{B}_x$ films of 100 nm thickness with x = (a) 0, (b) 5, (c) 10, and (d) 15.

observation direction. Figure 5 shows the $\Delta\ell/\ell_{\text{poly-crystalline/amorphous}}(\psi)$ measured for $(\mathrm{Fe}_{0.7}\mathrm{Co}_{0.3})_{100-x}\mathrm{B}_x$ films composed of poly-crystalline and/or amorphous phases prepared on VN poly-crystalline underlayers. The amplitudes of $\Delta\ell/\ell_{\text{poly-crystalline/amorphous}}(\psi)$ are smaller than those of $\Delta\ell/\ell_{[100]}(\varphi)$ and larger than those of $\Delta\ell/\ell_{[110]}(\varphi)$.

Figure 6 shows the magnetic field dependences of λ_{100}, λ_{111}, and $\lambda_{\text{poly-crystalline/amorphous}}$. The λ_{100} and λ_{111} values of film with x = 0 almost saturate at a low magnetic field of 25 Oe. The λ_{100} and λ_{111} values of film with x = 15 do not saturate at a magnetic field of 1200 Oe. On the other hand, the $\lambda_{\text{poly-crystalline/amorphous}}$ of films with x = 0–15 saturate at low magnetic fields around 25–50 Oe. The saturation behaviors of magnetostriction are consistent with those of magnetization which are shown in Fig. 3.

Figure 7 summarizes the B content dependences of λ_{100}, λ_{111}, λ_{cal}, and $\lambda_{\text{poly-crystalline/amorphous}}$ measured under a rotating field of 1200 Oe. Here, λ_{cal}, which is given as

$$\lambda_{\text{cal}} = \frac{2}{5}\lambda_{100} + \frac{3}{5}\lambda_{111}\ , \tag{5}$$

is the approximate magnetostriction value of isotropic material calculated by using λ_{100} and λ_{111}. The film with x = 0 consisting of bcc(001) single-crystalline phase shows a large λ_{100} value of +200 × 10^{-6}, similar to the case of $\mathrm{Fe}_{70}\mathrm{Co}_{30}$ film epitaxially grown on MgO(001)[9]. λ_{100} value increases to +310 × 10^{-6} by B atom addition of x = 5. With further increasing the B content, λ_{100} value begins to decrease. The result is considered to be partly

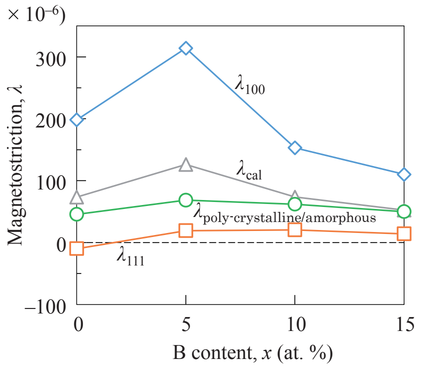

Fig. 7 B content dependences of λ_{100}, λ_{111}, λ_{cal}, and $\lambda_{poly\text{-}crystalline/amorphous}$ under a rotating field of 1200 Oe measured for $(Fe_{0.7}Co_{0.3})_{100-x}B_x$ films of 100 nm thickness.

due to unsaturation of magnetization at 1200 Oe and partly due to deterioration of magnetostriction caused by rough surface. λ_{111} value increases from a small negative value of -10×10^{-6} to a small positive value of $+20 \times 10^{-6}$ with increasing the B content from $x = 0$ to 5 and then stays almost constant from $x = 5$ to 15. As a result, a maximum value of λ_{cal} is recognized at $x = 5$. In contrast, the films composed of poly-crystalline and/or amorphous phases have similar $\lambda_{poly\text{-}crystalline/amorphous}$ values of around $+60 \times 10^{-6}$ for all the B contents. These results indicate that λ_{100} value of bcc(001) crystal does not decrease in the B content range of x = 0–15. It seems possible to prepare an $(Fe_{0.7}Co_{0.3})_{100-x}B_x$ film with larger λ_{100} value with the B content higher than $x = 10$ by reducing the surface roughness which may yield low H_c. The present study shows that B atom addition is effective in enhancing λ_{100} value and that it is important to prepare a thin film with reduced surface undulation in order to extract the intrinsic magnetostrictive property.

4. Conclusion

$(Fe_{0.7}Co_{0.3})_{100-x}B_x$ (x = 0–15, at. %) alloy films of 100 nm thickness are prepared on VN(001) single-crystalline underlayers at 600 °C and on VN poly-crystalline underlayers at RT. Single-crystalline films of bcc(001) orientation are obtained on VN single-crystalline underlayers, whereas poly-crystalline and/or amorphous films are formed on VN poly-crystalline underlayers, where the structure varies depending on the B content and the deposition temperature. The surface roughness, R_a, of single-crystalline film increases from 0.4 to 13 nm with increasing the B content from x = 0 to 15, while poly-crystalline and/or amorphous films possess flatter surfaces with the R_a lower than several nanometers. Good soft magnetic properties are observed for the films with flat surfaces, and surface roughness is shown to be an origin in increasing the coercivity. The single-crystalline film with x = 0 shows a large λ_{100} value, which is enhanced by B addition of x = 5 up to $+310 \times 10^{-6}$. As the B content further increases, the λ_{100} value decreases due to unsaturation of magnetization and increase in surface roughness. The λ_{111} values are nearly zero (-10×10^{-6} – $+20 \times 10^{-6}$) for all the investigated B contents. The films consisting of poly-crystalline and/or amorphous phases show moderately large λ values of about $+60 \times 10^{-6}$ for all the B contents. The present study has shown that B addition as well as realization of flat surface are important factors in enhancing the magnetostriction.

Acknowledgements This paper is based on results obtained from a project, 20002152-0, subsidized by the New Energy and Industrial Technology Development Organization. Authors thank Mr. Naoki Yoshihara and Ms. Yuko Kaneda of Instrumental Analysis Center at Yokohama National University for their excellent technical supports for EDS, XPS, and XRD measurements.

References

1) R. M. Bozorth: *Ferromagnetism*, p. 194 (Van Nostrand, New York, 1964).
2) S. Chikazumi: *Physics of Ferromagnetism*, p. 111 (Syokabo, Tokyo, 1961).
3) H. M. A. Urquhart, K. Azumi, and J. E. Goldman: *DTIC Tech. Rep.*, no. AD0018771 (1953).
4) R. C. Hall: *J. Appl. Phys.*, **30**, 816 (1959).
5) R. C. Hall: *J. Appl. Phys.*, **31**, S157 (1960).
6) S. Chikazumi: *Physics of Ferromagnetism*, p. 122 (Syokabo, Tokyo, 1961).
7) T. Nakajima, T. Takeuchi, I. Yuito, K. Kato, M. Saito, K. Abe, T. Sasaki, T. Sekiguchi, and S. Yamaura: *Mater. Trans.*, **55**, 556 (2014).
8) D. Hunter, W. Osborn, K. Wang, N. Kazantseva, J. Hattrick-Simpers, R. Suchoski, R. Takahashi, M. L. Young, A. Mehta, L. A. Bendersky, S. E. Lofland, M. Wuttig, and I. Takeuchi: *Nat. Commun.*, **2**, 518 (2011).
9) K. Serizawa, M. Ohtake, T. Kawai, M. Futamoto, F. Kirino, and N. Inaba: *J. Magn. Soc. Jpn.*, **43**, 50 (2019).
10) C. L. Platt, N. K. Minor and T. J. Klemmer: *IEEE Trans. Magn.*, **37**, 2302 (2001).
11) D. Wang, C. Nordman, Z. Qian, J. M. Daughton, and J. Myers: *J. App. Phys.*, **97**, 10C906 (2005).
12) J. Díaz, C. Quirós, L. M. Alvarez-Prado, C. Aroca, R. Ranchal, M. Ruffoni, and S. Pascarelli: *Phys. Rev. B*, **85**, 134437 (2012).
13) J. Hayakawa, S. Ikeda, F. Matsukura, H. Takahashi and H. Ohno: *Jpn. J. Appl. Phys.*, **44**, L587 (2005).
14) R. S. Turtelli, J. P. Sinnecker, R. Grössinger, G. Badurek, C. Kussbach, and P. Allia: *Phys. Rev. B*, **63**, 094427 (2001).
15) J. P. Sinnecker, R. S. Turtelli, R. Grössinger, G. Badurek, P. Riedler, and S. Menhart: *J. App. Phys.*, **85**, 1043 (1999).
16) J. A. Venable: *Introduction to surface and thin film process* (Cambridge Univ. Press, New York, 2000).
17) R. Nakanishi, S. Kunitsugu, and K. Sueoka: *J. Surf. Finish. Soc. Jpn.*, **61**, 535 (2010).
18) L. Vitos, A. V. Ruban, H. L. Skriver, and J. Kollár: *Surf. Sci.*, **411**, 186 (1998).
19) T. Shimizu, M. Ohtake, M. Futamoto, F. Kirino, and N. Inaba: *J. Magn. Soc. Jpn.*, **43**, 109 (2019).
20) T. Kawai, M. Ohtake, and M. Futamoto: *Thin Solid Films*, **519**, 8429 (2011).
21) M. Aldén, H.L. Skriver, S. Mirbt, and B. Johansson: *Surf. Sci.*, **315**, 157 (1994).
22) E. N. Eremin, V. M. Yurov, V. Ch. Laurynas, S. A. Guchenko, and S. S. Kasymov: *J. Phys.: Conf. Ser.*, **1210**, 012041 (2019).
23) S. Ma, N. Zong, H. Dong, and T. Jing: *IOP Conf. Ser.: Mater. Sci. Eng.*, **861**, 01204 (2020).

Received Mar. 31, 2021; Revised Jul. 9, 2021; Accepted Sep. 16, 2021

J. Magn. Soc. Jpn., **45**, 142-148 (2021)

<Paper>

Magnetism and Astronomical Infrared Spectrum of Fullerene C_{60} and Void Induced Graphene Molecules

Norio Ota[1], Aigen Li[2], Laszlo Nemes[3] and Masaaki Otsuka[4]

[1]Graduate school of Pure and Applied Sciences, University of Tsukuba, *1-1-1 Tennodai, Tsukuba-City Ibaraki, 305-8571, Japan*
[2]Department of Physics and Astronomy, University of Missouri, *Columbia, MO 65211, USA*,
[3]Research Center for Natural Sciences, Ötvös Lóránd Research Network, *Budapest 1519, Hungary*
[4]Okayama Observatory, Kyoto University, *Asakuchi Okayama, 719-0232, Japan.*

Fullerene C_{60} shows astronomical four infrared bands (IR) of carbon rich planetary nebulae. However, there remain many unidentified bands. Our previous paper revealed that single void-defect induced graphene molecule reproduce many astronomical bands. In this paper, we investigated a series of multiple-void induced graphene molecules. We tried spin dependent DFT calculation. Model molecules are C_{23} (one carbon pentagon ring among hexagon network), C_{22} (two), and C_{21} (three). Those were all magnetic molecules with spin state of Sz =2/2, 2/2 and 4/2 respectively. Calculated IR was compared with astronomical observation. The largest astronomical band at 18.9 micrometer was found in C_{23}. Second largest band at 17.4 micrometer appeared both in C_{22} and C_{21}. Other major bands from 6 to 10 micrometer were reproduced well by a combination of C_{23}, C_{22} and C_{21}. Similarly, larger size graphene molecules of C_{53}, C_{52} and C_{51} were also magnetic and reproduced astronomical bands as well. Weighting sum IR of those molecules could successfully trace astronomical 12 bands from 6 to 20 micrometer. A series of multiple void induced graphene would be major component of astronomical carbon. Fullerene C_{60} would be one of them.

Key words: graphene, fullerene C_{60}, spin state, DFT, infrared spectrum

1. Introduction

It is well known that fullerene C_{60} [1)] shows astronomical infrared bands (IR). In 2010, Cami et al.[2)] reported the presence of C_{60} in astrophysical environments by the detection of a set of four bands at 7.0, 8.45, 17.3 and 18.9 µm. Many studies are following it [3)- 8)]. Typical astronomical objects are the Galactic planetary nebula Tc1 [2)] and the Small Magellanic Cloud nebula Lin49 [9)]. Observed spectra were 12 bands, which were compared with experiment and theory [10)- 12)]. There remain many unidentified bands not explained by C_{60}. It is also well known that graphene is a raw material for synthesizing fullerene [13), 14)]. Otsuka et al.[9)] suggested the presence of small graphene in space. Graphene was experimentally synthesized by Geim and Novoselov [15)].

Our recent study on graphene molecule by the density functional theory (DFT) shows that single void-defect on carbon hexagon network brings highly polarized spin configuration and structure change [16), 17)], and finally brings drastic change of molecular vibrational IR. Such result was understood based on pure carbon magnetism [18)- 24)]. Model molecules were C_{23} and C_{53}, which has one carbon pentagon ring among hexagons. It was firstly revealed that calculated IR shows good coincidence with astronomically observed one. Also, calculation show rough coincidence with the laser induced carbon plasma experiment [25)- 28)]. Those molecules were magnetic with spin-state of Sz =2/2. Calculated IR of C_{23} and C_{53} could reproduce astronomically observed one of carbon rich nebulae Tc1 and Lin49. However again, there remain some unidentified bands, especially second largest band at 17.4 µm. We should do advanced study on nano-carbon candidates.

Here is an interesting idea that we should study multiple void induced graphene molecules, because fullerene C_{60} has 12 carbon pentagon rings combined with 20 hexagons. Such multiple pentagon rings could be induced from multiple voids on graphene sheet. In 2013, Tielens opened such concept under the name of top-down-process in his review article [29)]. In this study, we investigate a series of multiple void induced graphene molecules focusing on spin-state and molecular vibrational IR. Results will be compared with astronomical observation and laboratory experiment. This paper is a joint study by different research field, which would develop a new science field named as like the Astro-magnetism.

2. Calculation Method

In calculation, we used DFT [30), 31)] with the unrestricted B3LYP functional [32)]. We utilized the Gaussian09 software package [33)] employing an atomic orbital 6-31G basis set. Unrestricted DFT calculation was done to have the spin dependent atomic structure. The required convergence of the root-mean-square density matrix was 10^{-8}. Based on such optimized

---

Corresponding author: Norio Ota (n-otajitaku@nifty.com).

molecular configuration, fundamental vibrational modes were calculated, such as carbon to carbon (C-C) stretching modes, (C-C) bending modes and so on, using the same Gaussian09 33). This calculation also gives harmonic vibrational frequency and intensity in infrared region. The standard scaling is applied to the frequencies by employing a scale factor of 0.975 for pure carbon system taken from the laboratory experimental value of 0.965 based on coronene-molecule of $C_{24}H_{12}$ 34). Correction due to anharmonicity was not applied to avoid uncertain fitting parameters. To each spectral line, we assigned a Gaussian profile with a full width at half maximum of 4cm^{-1}. Any molecular symmetricity was not applied to compare delicate change of molecular configuration and compare small difference of total energy.

3. Fullerene C_{60} and Graphene C_{23}

3.1 Stable spin state

Input parameters for DFT are charge and spin parameter Sz. Charge was zero (neutral) for every case. We dealt total molecular spin S (vector). Molecule is rotatable material, easily follows to the external magnetic field of z-direction. Projected component Sz to z-direction is a good quantum number.

Result of C_{60} is illustrated in Fig. 1. Total molecular energy of Sz =0/2 is 1.79 eV lower than that of Sz =2/2. Stable spin-state was nonmagnetic one of Sz =0/2, which is contrary to previously reported graphene molecule of C_{23} 16) with magnetic Sz =2/2. We note again here the creation step of C_{23}. As illustrated in Fig. 2, starting molecule was C_{24} having seven carbon hexagon rings. High-speed particle may attack one carbon atom and kick it out. Single void will be created. There occurs re-bonding between carbon atoms. Resulted molecule was C_{23} having one pentagon ring. Initial void-defect holds 3 radical carbons and allows 6 spins. Six spins make capable spin-states of Sz =0/2, 2/2, 4/2 and 6/2. Among them, calculated energy of Sz =4/2 and 6/2 show unstable high energy. Here, we should compare Sz =0/2 and 2/2. It should be noted that molecular energy of Sz =2/2 was 0.64 eV lower (stable) than Sz =0/2. We can see up-spin major spin cloud for Sz =2/2 as illustrated on bottom right of Fig. 2 at a cutting surface of spin density 10 e/nm^3. We can see up-spin cloud (by red) at a pentagon site.

3.2 Infrared spectrum

Comparison of calculated IR with astronomically observed one is important. Both DFT targeted molecule and interstellar molecule have common condition, that is, of ultra-low material density and of low temperature. Laboratory experiment on earth cannot realize such conditions. Otsuka et al.9) opened astronomically observed bands as illustrated in Fig. 3 on top for Tc1 nebula by red and for Lin49 by blue. Laboratory gas-phase experiment for C_{60} by Nemes et al.26) was marked by blue arrows on middle. Calculated spectrum of C_{60} was illustrated for Sz =0/2 by green and for Sz =2/2 by light green. It should be noted that the observed spectra are seen in emission, while DFT gives absorption. A star may illuminate the molecule and excites them to give rise infrared emission. Detailed discussion was done by Li and Drain 35), 36). We regard that DFT calculated absorbed spectrum is a mirror image of emission one in case of sufficient high energy excitation.

Calculated spectrum of Sz =2/2 of C_{60} shows so ambiguous as illustrated on bottom of Fig. 3. Whereas for stable spin-state Sz =0/2, we can see specific four bands.

In Table 1, every IR obtained by experiment, astronomical observation and DFT calculation were listed in detail. Calculated largest band of C_{60} is 18.7 μm, which is 0.1 μm shorter than gas-phase laboratory experiment of 18.8 μm. Whereas, astronomically observed band was 18.9 μm. There remains a question that astronomical 18.9 μm band would come from C_{60} or not. Because, in our previous study, single void induced C_{23} show a band just at 18.9 μm.

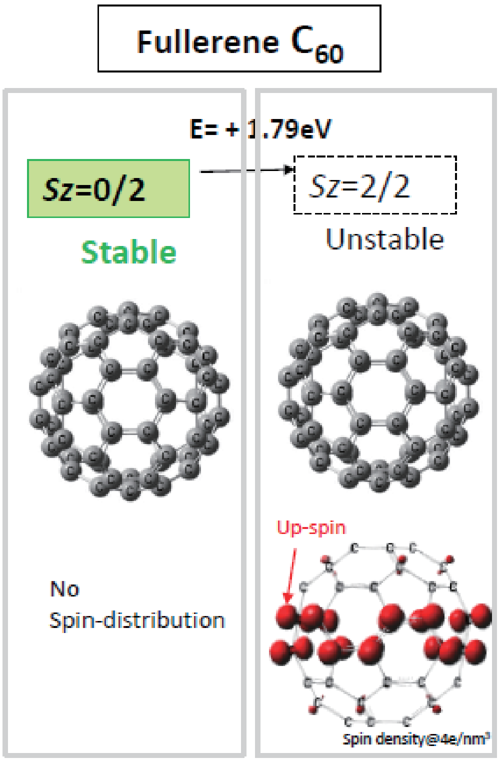

Fig. 1 Spin state of fullerene C_{60} by DFT calculation.

Table 1 Infrared spectrum of C_{60} and graphene molecules

Laboratory Experiment			Astronomical Observation		DFT Calculation (0 K, Isolate molecule)							
C60 Gas-phase (Extrapolated to 0 K)	C60 Solid (300K)	Laser induced carbon (300K)	Tc1 Nebula	Lin49 Nebula	C60 Sz=0/2	C24 Sz=0/2	C23 Sz=2/2	C22 Sz=2/2	C21 Sz=4/2	C53 Sz=2/2	C52 Sz=2/2	C51 Sz=2/2
Number of carbon rings hexagon: 20 pentagon: 12		– –			20 12	7 0	6 1	5 2	4 3	18 1	17 2	16 3
(Wavelength in micrometer)												
						20.1		19.8			19.6	
												19.1
							19.1	19.2				
	18.93		18.9 µm	18.9			18.9	19.0		18.9	18.9	
18.82					18.72							
												18.6
17.41	17.33		17.4	17.4	17.44		17.4	17.3	17.4			
							16.9					
				16.6			16.5					
								16.4				
				14.3			14.3			14.3		
				13.9						13.9	13.8	
											13.5	
				13.3						13.4	13.3	13.1
									12.7			
											11.4	
		10.2		10.0			9.9	10.2				
		9.5				9.8					9.3	
			9.0				9.0	8.9	8.9			9.0
										8.6		
8.40	8.45		8.4	8.4	8.58						8.4	8.3
		8.3										
				8.1				8.1				
							8.0	7.9	7.9			
		7.7	7.6	7.6				7.5	7.6	7.6	7.6	7.6
		7.4					7.4			7.3		
6.97	7.00	Plateau	7.1	7.1			7.1		7.2	7.1	7.1	7.0
		(5.9–7.7)						6.9				
		6.7	6.5	6.6	6.77	6.6	6.6			6.5		6.5
										6.3	6.3	
		5.9										

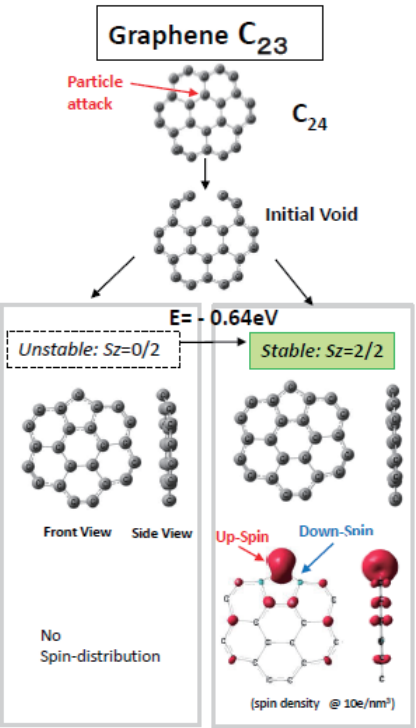

Fig. 2 Spin state of single void induced graphene C_{23}.

In Fig. 4, sharp astronomical emission peak at 18.7 µm (marked by black arrow) is a strong atomic emission line of S_{III}. We are afraid that such strong atomic line may hide a band of C_{60}.

Calculated band of C_{60} at 17.4 µm coincides well both with astronomical Band-B (17.4 µm) and with gas-phase laboratory experiment at 17.4 µm [26].

In shorter wavelength region, calculated C_{60} show a band at 6.77 µm. It was 0.2 µm shorter than experimental bands of 6.97 µm. Cami et al. suggested that Band-L at 7.1 µm comes from C_{60}. However, it was strange that in our previous paper [16], graphene C_{23} show just 7.1 µm band. Gas phase experiment also has some difficulty. Experiment was done at temperature from 850 to 1150 K and simply extrapolated to 0 K, which has a gap of five order weak strength. Under such complicated situation, we need advanced study.

Cami et al.[2] also suggested possibility of fullerene C_{70}. Astronomical bands would be explained by mixing C_{70} and C_{60}. However, bands of C_{70} were 18.7, 17.3, 15.5 and 14.8 µm. They could not explain observed major bands from 6 to 13 µm.

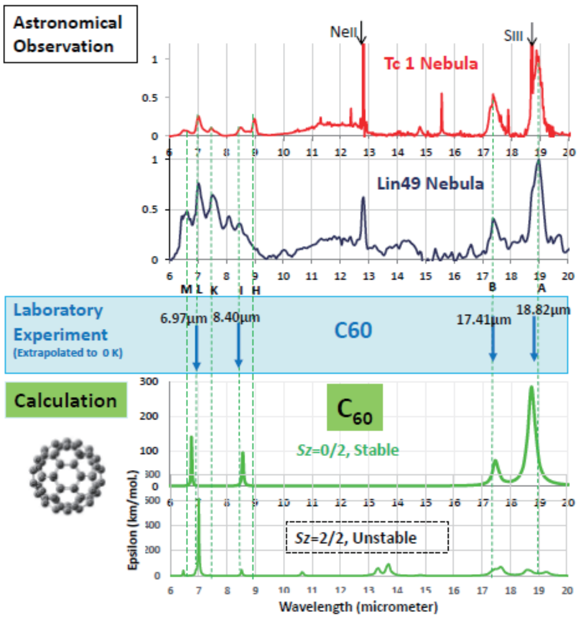

Fig. 3 Comparison of IR of fullerene C_{60} by astronomical observation, laboratory experiment and DFT calculation.

As shown in Fig. 4, we can see many astronomical bands from Band-A to M. Our previous results [16)] are again illustrated in Fig. 4. Major band of C_{23} has twin peaks at 18.9 and 19.0 μm, also C_{53} has single peak at 18.9 μm, which are just related to observed Band-A. Second major Band-B was seen at 17.4 μm, which was reproduced well by calculated C_{60}. However unfortunately, C_{23} and C_{53} show weak intensity at 17.4 μm.

At shorter wavelength region from 6 to 10 μm, calculated spectrum of C_{60} only show two bands at positions of Band-I and M. While graphene C_{23} and C_{53} show many bands to coincide well with astronomical bands of Band-G, H, I, J, K, L and M. Moreover, C_{53} could reproduce further detailed bands coincide with astronomical Band-D, E, F.

4. Multiple-Void Induced Graphene Molecules

4.1 Stable spin state

Fullerene C_{60} has 12 carbon pentagon rings among 20 hexagons. Multiple pentagon rings could be realized from multiple voids. In this study, we assumed multiple voids for multiple carbon pentagons. We started from C_{24} as illustrated in Fig. 5. Single void could induce C_{23} with one pentagon ring marked by red circled 5. Two-voids induced C_{22} has two pentagons. Molecular configuration was umbrella like curved structure as shown by side view. Three voids induced C_{21} also show umbrella like configuration. Origin of such structure was discussed by Ota [37)] based on re-bonding between carbon atoms by mixing sp^2-orbit with sp^3. Also, Galue & Leines [38)] discussed the π-electron irregularity.

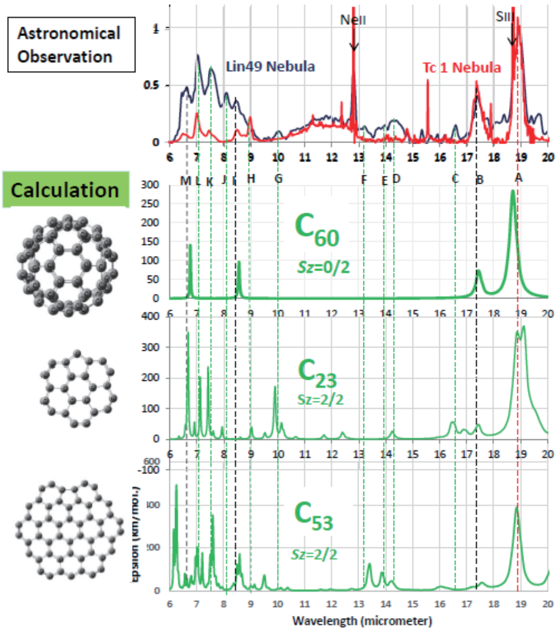

Fig. 4 DFT calculated molecular vibrational spectra of (C_{60}, $Sz=0/2$), (C_{23}, $Sz=2/2$) and (C_{53}, $Sz=2/2$) compared with astronomically observed spectra of carbon rich nebulae Tc1 and Lin49.

As shown in Fig. 6, possible spin states of C_{22} are $Sz=0/2$. 2/2 and 4/2. Most stable state was $Sz=2/2$, which energy was 0.17 eV lower than $Sz=4/2$ and 1.06 eV lower than $Sz=0/2$. Spin-distribution was illustrated on right. Similarly, C_{21} has three pentagons. Stable spin state was $Sz=4/2$. In every molecule, there arises up-spin cloud (by red) at pentagon carbon atom.

Size dependence was checked. Large size molecules starting from C_{54} were analyzed as shown in Fig. 7. Single void induced molecule of C_{53} show stable spin-state of $Sz=2/2$. Spin configuration was complex as illustrated on right column. Two voids induced C_{52} has two carbon pentagon rings and show stable spin state of $Sz=2/2$. Similarly, three voids induced C_{51} has three pentagons and show stable spin-state of $Sz=2/2$.

4.2 Infrared spectrum

In Fig. 8, calculated IR were illustrated for molecules of (C_{23}, $Sz=2/2$), (C_{22}, $Sz=2/2$) and (C_{21}, $Sz=4/2$). It should be noted that Band-B at 17.4 μm (marked by a red broken line) was reproduced well by two voids induced C_{22}, also by three voids induced C_{21}. Other detailed bands were well reproduced by C_{22} and C_{21}.

In Fig. 9, calculated spectra of C_{54} family are illustrated. Both on C_{53} and C_{52}, we can see the largest band at 18.9 μm, which just coincide with Band-A. Unfortunately, we could not find any large intensity at 17.4 μm of Band-B. Number of pentagon rings to hexagons may contribute to the intensity at 17.4 μm.

At middle wavelength region, Band-D, E, and F were reproduced by C_{54} family. Also at shorter region, Bands from H to M were reproduced well. While calculated band at 6.2 μm was not shown by observation. We are afraid of the sensitivity at 6.2 μm, because detection range of Spitzer/IRS spectra was 6 to 9 μm

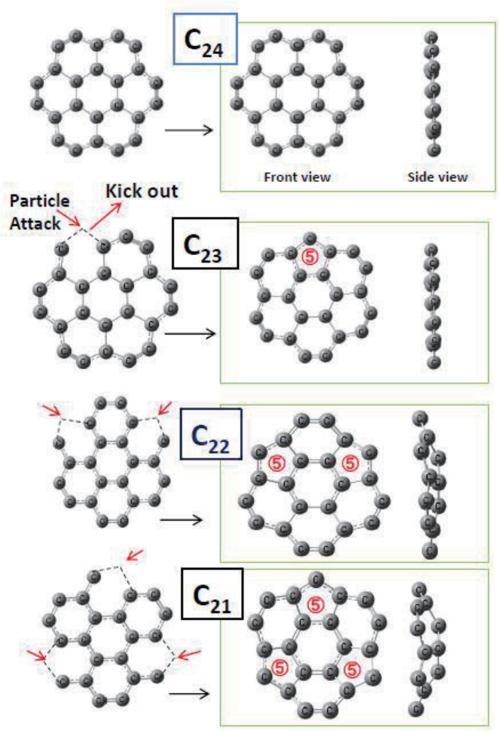

Fig. 5 Creation of multi-void induced C_{24} family.

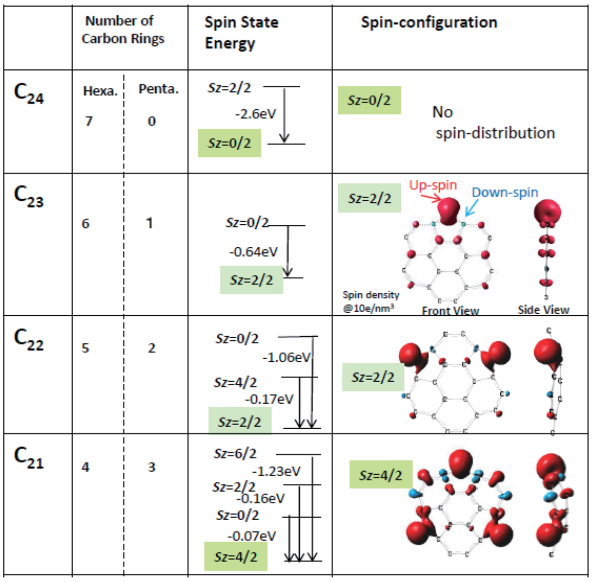

	Number of Carbon Rings Hexa.	 Penta.	Spin State Energy	Spin-configuration
C_{24}	7	0	Sz=2/2 -2.6eV Sz=0/2	Sz=0/2 No spin-distribution
C_{23}	6	1	Sz=0/2 -0.64eV Sz=2/2	Sz=2/2 Up-spin Down-spin Spin density @10e/nm³ Front View Side View
C_{22}	5	2	Sz=0/2 -1.06eV Sz=4/2 -0.17eV Sz=2/2	Sz=2/2
C_{21}	4	3	Sz=6/2 -1.23eV Sz=2/2 -0.16eV Sz=0/2 -0.07eV Sz=4/2	Sz=4/2

Fig. 6 Stable spin state of graphene C_{24} family.

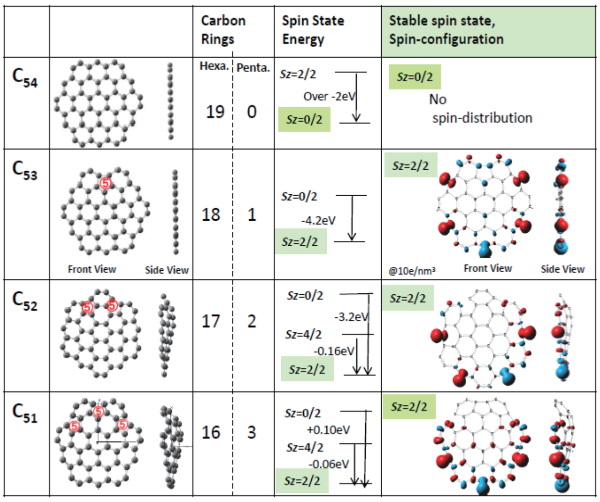

		Carbon Rings Hexa.	 Penta.	Spin State Energy	Stable spin state, Spin-configuration
C_{54}		19	0	Sz=2/2 Over -2eV Sz=0/2	Sz=0/2 No spin-distribution
C_{53}	⑤ Front View Side View	18	1	Sz=0/2 -4.2eV Sz=2/2	Sz=2/2 @10e/nm³ Front View Side View
C_{52}	⑤ ⑤	17	2	Sz=0/2 -3.2eV Sz=4/2 -0.16eV Sz=2/2	Sz=2/2
C_{51}	⑤ ⑤ ⑤	16	3	Sz=0/2 +0.10eV Sz=4/2 -0.06eV Sz=2/2	Sz=2/2

Fig. 7 Stable spin-state of larger size graphene C_{54} family.

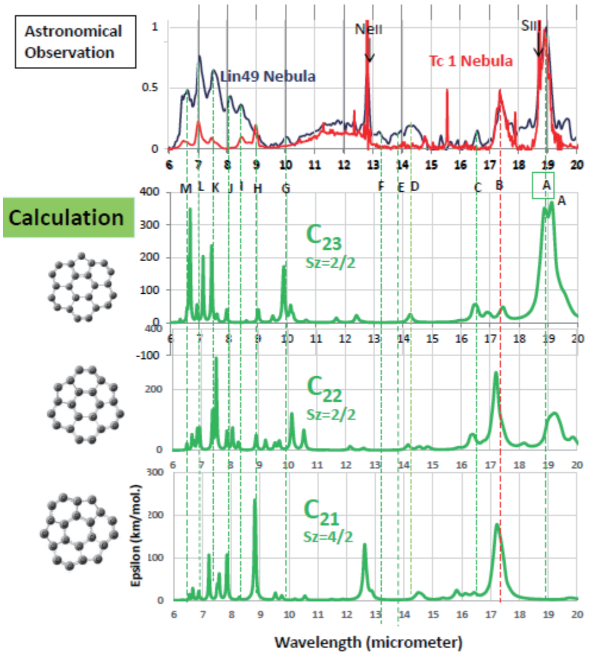

Fig. 8 Calculated IR of (C_{23}, Sz =2/2), (C_{22}, Sz =2/2) and (C_{21}, Sz =4/2) compared with observation. Band-B was well reproduced by C_{22} and C_{21}.

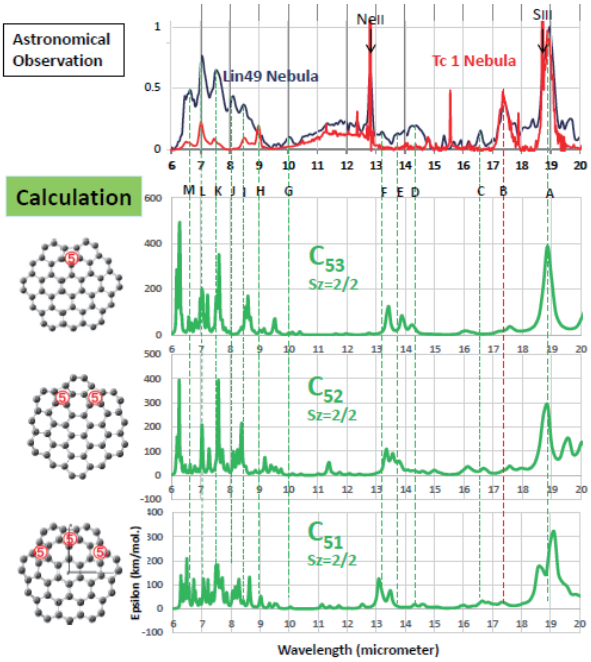

Fig. 9 Calculated spectra of (C_{53}, Sz =2/2), (C_{52}, Sz =2/2) and (C_{51}, Sz =2/2) compared with observation.

5. Weighting Sum IR

As discussed in a previous section, C_{60} was difficult to reproduce full bands of astronomical bands as shown on panel (C) in Fig. 10. A series of multiple void induced graphene has a capability to reproduce full bands. We tried a weighting sum spectrum by C_{23}, C_{22}, C_{53}, and C_{52}. It was demonstrated on panel (D). Observed major bands of Band-A and B were well reproduced. Also detailed bands of Band-C, D, E, F, were reproduced well. Shorter wavelength bands of Band-G, I, K, L and M were well reproduced again. In panel (E), we add spectrum of C_{60} to above weighting sum of graphene. It looks that major part of (E) was similar with (D). There is not any significant difference. Major contribution of astronomically observed spectrum may come from graphene. Fullerene C_{60} would contribute a part of them.

6. Laser Induced Carbon Plasma Experiment

As an analogy of astronomical creation of carbon dust, the laser induced carbon plasma experiment (LICP) was done. High power laser irradiates bulk graphite to create carbon plasma and finally creates nano-carbon [25]. In third column of Table 1, IR by LICP was noted.

In Fig. 11, we can see rough coincidence of LICP spectrum with calculated weighting sum IR of C_{23}, C_{22}, C_{53} and C_{52}. While as marked on middle, there was little coincidence with gas-phase experimental two bands of C_{60} [28].

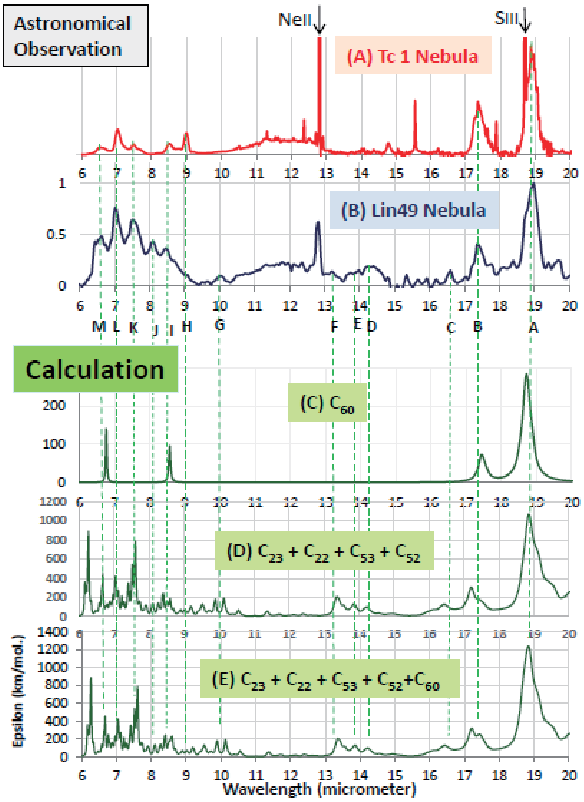

Fig. 10 Astronomical spectrum were compared with calculated one of C_{60} in (C), with weighting sum spectrum of C_{23}, C_{22}, C_{53} and C_{52} in (D). Further addition of C_{60} is illustrated in (E).

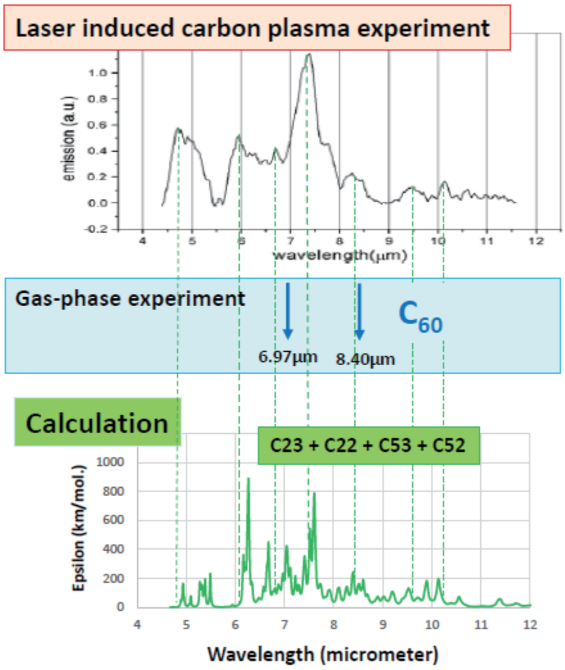

Fig. 11 Infrared spectrum of the laser induced carbon plasma experiment was roughly explained by weighting sum IR of C_{23}, C_{22}, C_{53} and C_{52}.

7. Conclusion

A series of multiple void induced graphene molecules were studied by DFT calculation comparing with astronomical observation and laboratory experiments.

(1) Fullerene C_{60} gives astronomically observed IR. We could obtain four bands by calculation. However, there remain many unidentified astronomical bands.

(2) Single void-defect induced graphene molecule reproduced well many bands. However, there remain major astronomical band at 17.4 µm.

(3) A series of multiple-void induced graphene molecules were studied. Model graphene were C_{23} (one void induced one pentagon ring), C_{22} (two), C_{21} (three). Stable spin state was Sz =2/2, Sz =2/2 and Sz =4/2 respectively.

(4) The largest band at 18.9 µm was found in C_{23}. Second largest band at 17.4 µm was seen both in C_{22} and C_{21}.

(4) Similarly, large size graphene C_{53}, C_{52} C_{51} could also reproduce astronomical bands as well.

(5) Weighing sum IR by C_{23}, C_{22}, C_{53} and C_{52} could successfully trace observed 12 bands from 6 to 20 µm.

(6) Laboratory experiment of laser induced carbon plasma suggested rough coincidence of spectrum with a weighing sum IR by C_{23}, C_{22}, C_{53} and C_{52}.

A series of multiple void induced graphene molecules would be a major component of astronomical carbon dust. Fullerene C_{60} would be a part of them.

Acknowledgement Aigen Li is supported in part by NSF AST-1311804 and NASA NNX14AF68G.

References

1) H. W. Kroto, J. R. Heath, S. C. Obrien, R. F. Curl, and R. E. Smalley: *Nature*, **318**, 162 (1985).
2) J. Cami, J. Bernard-Salas, E. Peeters and S. E. Malek: *Science,* **329**, 1180 (2010).
3) K. Sellgren, M. W. Werner, J. G. Ingalls, J. D. T. Smith, T. M. Carleton and J. Christine: *ApJL,* **722**, L54 (2010).
4) Y. Zhang, & S. Kwok: *ApJ*, **730**, 126 (2011).
5) O. Bern´e & A. G. G. M.Tielens: *PNAS*, **109,** 4010 (2012) Also, Bern´e, N. L. J. Cox, G. Mulas & C. Joblin: *A&A,* **605**, L1 (2017).
6) D. A. Garc´ıa-Hern´andez, A. Manchado, P. Garc´ıa-Lario, et al.: *ApJL,* **724**, L39 (2010).
7) M. C. Martin, D. Koller, and L. Mihaly: *Phys. Rev.* **B47**, 14607 (1993).
8) J. Fabian: *Phys. Rev.* **B53**, 13864 (1996).
9) M. Otsuka, F. Kemper, M. L. Leal-Ferreira, M. L. Aleman, M. L. Bernard-Salas, J. Cami, B. Ochsendorf, E. Peeters, and P. Scicluna: *MNRAS*, **462,** 12 (2016).
10) A. Candian, M. G. Rachid, H. MacIssac, V. N. Staroverov, E. Peeters, and J. Cami: preprint from web site of *ResearchGate* by Allessandra Candians, titled "Searching for stable fullerenes in space with computational chemistry" (2009).
11) H.W. Kroto & K. McKay: *Nature*, **331**, 328 (1988).
12) A. Chuvilin, U. Kaiser, E. Bichoutskaia, N. A. Besley, & A.N. Khlobystov: *Nature Chem.*, **2**, 450 (2010).
13) H.W. Kroto & K. McKay: *Nature*, **331**, 328 (1988).
14) A. Chuvilin, U. Kaiser, E. Bichoutskaia, N. A. Besley, & A.N. Khlobystov: *Nature Chem.*, **2**, 450 (2010).
15) A. K. Geim & K. S. Novoselov: *Nature Materials,* **6**, 183 (2007).
16) N. Ota, A. Li, L. Nemes and M. Otsuka: *J. Magn. Soc. Jpn.*, **45**, 41 (2021).
17) N. Ota: *arXiv*, 1811.05043 (2018)
18) P. Esquinazi, D. Spemann, R. Hohne, A.Setzer, K. Han, and T. Butz: *Phys. Rev. Lett.*, **91**, 227201 (2003).
19) J. Cervenka, M. Katsnelson and C. Flipse: *Nature Phys.,* **5,** 840 (2009), (https://doi.org/10.1038/nphys1399).
20) K. Kusakabe and M. Maruyama: *Phys. Rev. B*, **67**, 092406 (2003).
21) N. Ota, N. Gorjizadeh and Y. Kawazoe: *J. Magn. Soc. Jpn.*, **35**, 414 (2011), also **36**, 36 (2012).
22) N. Ota: *J. Magn. Soc. Jpn.*, **37**, 175 (2013).
23) T. Kondo, Y. Honma, J. Oh, T. Machida, and J. Nakamura: *Phys. Rev. B*, **82**, 153414 (2010).
24) N. Ota and L. Nemes: *J. Magn. Soc. Jpn.*, **45**, 30 (2021).
25) L. Nemes, E. Brown, S. C. Yang, U. *Hommerrich: Spectrochimica Acta Part A, Molecular and Biomolecular Spectroscopy,* **170**, 145 (2017).
26) L. Nemes, R. S. Ram, P. F. Bernath, F. A. Tinker, M. C. Zumwalt, L. D. Lamb, D. R. Huffman: *Chem. Phys. Lett.*, **218**, 295 (1994).
27) W. Kratschmer, L. D. Lamb, K. Fostiropoulos and D. R. Huffman: *Nature,* **347**, 354 (1990).
28) L. Nemes, A. Keszler, J. Hornkohl, and C. Parigger: *Applied Optics*, **44-18**, 3661 (2005).
29) A. G. Tielens: *Rev Mod. Phys.*, **85**, 1021 (2013).
30) P. Hohenberg and W. Kohn: *Phys. Rev.*, **136**, B864 (1964).
31) W. Kohn and L. Sham: *Phys. Rev.*, **140**, A1133 (1965).
32) A. Becke: *J. Chem. Phys.*, **98**, 5648 (1993).
33) M. Frisch, G. Trucks, H. Schlegel et al: Gaussian 09 package software, Gaussian Inc. Wallington CT USA (2009).
34) N. Ota: for $C_{24}H_{12}$ on *arXiv,* 1412.0009 (2014), for scaling factor on *arXiv,* 1502.01766.
35) A. Li and B. T. Draine: *ApJ,* **554**, 778 (2001).
36) B. T. Draine and A. Li: *ApJ,* **551**, 807 (2001).
37) N. Ota: *arXiv,* 1808.01070 (2018).
38) H. Galue, and G. Leines: *Phys. Rev. Lett.,* **119**, 171102 (2017).

Note on abbreviation of astronomical journals,
ApJ: The Astrophysical Journal
ApJL: The Astrophysical Journal Letters
A&A: Astronomy and Astrophysics
MNRAS: Monthly Notices of the Royal Astronomical Society
PNAS: Proceedings of the National Academy of Sciences

Received June 4, 2021; Revised July 23, 2021; Accepted Sept. 30, 2021

Editorial Committee Members・Paper Committee Members

Notice for Photocopying

If you wish to photocopy any work of this publication, you have to get permission from the following organization to which licensing of copyright clearance is delegated by the copyright owner.

〈All users except those in USA〉
Japan Academic Association for Copyright Clearance, Inc.（JAACC）
6–41 Akasaka 9-chome, Minato-ku, Tokyo 107–0052 Japan
Phone 81–3–3475–5618 FAX 81–3–3475–5619 E-mail: info@jaacc.jp

〈Users in USA〉
Copyright Clearance Center, Inc.
222 Rosewood Drive, Danvers, MA01923 USA
Phone 1–978–750–8400 FAX 1–978–646–8600

編集委員・論文委員

複写をされる方へ

当学会は下記協会に複写複製および転載複製に係る権利委託をしています．当該利用をご希望の方は，学術著作権協会（https://www.jaacc.org/）が提供している複製利用許諾システムもしくは転載許諾システムを通じて申請ください．ただし，本誌掲載記事の執筆者が転載利用の申請をされる場合には，当学会に直接お問い合わせください．当学会に直接ご申請いただくことで無償で転載利用いただくことが可能です．

権利委託先：一般社団法人学術著作権協会
〒107–0052 東京都港区赤坂9–6–41 乃木坂ビル
電話（03）3475–5618 FAX（03）3475–5619 E-mail: info@jaacc.jp

Journal of the Magnetics Society of Japan
Vol. 45 No. 6 (通巻第318号) 2021年11月1日発行

Vol. 45 No. 6 Published Nov. 1, 2021
by the Magnetics Society of Japan
Tokyo YWCA building Rm207, 1–8–11 Kanda surugadai, Chiyoda-ku, Tokyo 101–0062
Tel. +81–3–5281–0106 Fax. +81–3–5281–0107

Printed by JP Corporation Co., Ltd.
Sports Plaza building 401, 2–4–3, Shinkamata Ota-ku, Tokyo 144–0054
Advertising agency: Kagaku Gijutsu-sha

発行：(公社)日本磁気学会 101–0062 東京都千代田区神田駿河台 1–8–11 東京YWCA会館 207 号室
製作：ジェイピーシー 144–0054 東京都大田区新蒲田 2–4–3 スポーツプラザビル401 Tel.（03）6715–7915
広告取扱い：科学技術社 111–0052 東京都台東区柳橋 2–10–8 武田ビル4F Tel.（03）5809–1132